# Delayed Stormflow Generation in a Semi-humid Forested Watershed Controlled by Soil Water Storage and Groundwater Dynamics

Zhen Cui, Fuqiang Tian*

Department of Hydraulic Engineering, State Key Laboratory of Hydroscience and Engineering, Tsinghua University, Beijing 100084, China.

Corresponding author: Fuqiang Tian (tianfq@tsinghua.edu.cn)

**Key Points:**

- Threshold dynamics between soil water content and groundwater levels govern delayed stormflow generation.
- Groundwater fluctuations regulate the timing, magnitude, and merging of delayed and direct stormflow peaks.
- Hydrological connectivity and hydraulic conductivity increase with rising groundwater levels, driving delayed stormflow.

## Abstract

Recent research by Cui et al. (2024) identified a distinct threshold governing bimodal rainfall-runoff events in a semi-humid mountainous forested watershed in North China, where delayed stormflow appeared to be influenced by shallow groundwater dynamics. Building on these findings, this study delves deeper into the mechanisms driving these bimodal events, focusing on the interactions between soil water content (SWC) and groundwater level (GWL) during storm events. The results show that delayed stormflow is primarily governed by the interplay between SWC and GWL. Delayed stormflow is initiated when SWC exceeds the soil's water storage capacity, while its timing and magnitude further modulated by GWL fluctuations. During rainfall, SWC increases rapidly but stabilizes after the rain ceases if the soil's water-holding capacity is not reached. Conversely, when SWC surpasses the storage capacity, the excess rainwater infiltrates into the subsurface, recharging groundwater and causing a gradual rise in GWL. As GWL rises, enhanced hydraulic conductivity facilitates the lateral movement of shallow groundwater toward the stream channel, generating delayed stormflow. Concurrently, the effective connectivity between the stream channel and adjacent hillslopes increases in the vertical dimension. At higher GWL thresholds, GWL responses across the watershed become synchronized, significantly boosting groundwater discharge and reducing lag times. In extreme cases, the delayed stormflow peak converges with the direct stormflow peak. These findings advance the understanding of delayed stormflow mechanisms in semi-humid mountainous watersheds, contributing to refining runoff generation theories by providing insights into the threshold-driven processes that govern the timing and volume of delayed stormflow.



**Keywords:** Delayed stormflow; Soil water storage; Groundwater outflow; Stormflow generation mechanism; Hydraulic conductivity


## 1. Introduction

Stormflow processes in the Xitaizi Experimental Watershed (XEW), located in North China, exhibit a frequent occurrence of bimodal stormflow hydrographs (Fig. A1), which often lead to

significant stormflow and associated localized inundation. Analysis of 15 such events over the past decade revealed that the onset of these bimodal hydrographs is governed by threshold behavior. Specifically, delayed streamflow peaks tend to emerge when the combined total of event rainfall and antecedent soil moisture index exceeds 200 mm. The authors' findings suggest that shallow groundwater contributions are primarily responsible for these delayed stormflow events (Cui et al., 2024). However, the mechanisms behind the development of these bimodal hydrographs, which represent complex emergent hydrological behaviors, remain poorly understood. Understanding the formation of delayed stormflow is critical for advancing our comprehension of runoff generation processes and improving flood forecasting.

Bimodal hydrographs, characterized by dual streamflow peaks, typically occur during the wetting-up phases of catchments. Extensive research has identified several factors that influence dual streamflow peaks, including antecedent soil moisture, antecedent precipitation, groundwater levels, soil water storage, and rainfall amount (Haga et al., 2005; Graeff et al., 2009; Anderson and Burt, 1978; Padilla et al., 2015; Martínez-Carreras et al., 2016). Despite these advancements, the specific mechanisms that lead to threshold behavior and how these mechanisms produce the diverse shapes of stormflow hydrographs are still inadequately explained. For instance, Martínez-Carreras et al. (2016) found that a delayed peak only occurred when watershed storage reached a critical threshold of 113 mm. However, the precise reasons for this threshold and the underlying processes remain unclear.

The occurrence of bimodal hydrograph reflects a nonlinear runoff response, which offers valuable insights into the complex interactions between rainfall and runoff. The ~~Nonlinear~~ nonlinear pattern, characterized by~~including~~ both the timing and magnitude of the response, plays a crucial role in understanding stormflow processes. Recent decades have seen an increase in research on nonlinear and threshold changes in rainfall-runoff responses, contributing to a deeper understanding of stormflow generation mechanisms. Nonlinear patterns, often characterized by rapid runoff responses that may lead to flooding, have been extensively documented in recent decades (Detty and McGuire, 2010; Farrick and Branfireun, 2014; Graham et al., 2010; Tromp-van Meerveld and McDonnell,

2006a; Penna et al., 2011; Scaife et al., 2020). However, many studies fail to explore the intricate post-threshold mechanisms of these nonlinear shifts, leaving a gap in our understanding of stormflow generation across various catchments. While threshold behaviors are widely recognized, the detailed processes governing these shifts and their subsequent runoff dynamics remain underexplored.

Bimodal stormflow responses present an opportunity to investigate the relationship between rainfall thresholds and runoff generation, offering new perspectives on the timing and variability of stormflow. Despite this, many studies fail to distinguish between unimodal and bimodal streamflow responses. For example, Detty and McGuire (2010) focused on hydrological threshold responses but did not differentiate between unimodal and bimodal hydrographs, as their study primarily addressed general nonlinear rainfall-runoff processes in general. Similarly, Martínez-Carreras et al. (2016) observed delayed peaks and identified catchment storage as a key factor influencing streamflow responses, however, they did not explicitly differentiate the underlying mechanisms between unimodal and bimodal responses. ~~but did not further classify streamflow responses due to their focus on overall watershed storage conditions.~~ Such limitations often arise because the second peak in bimodal responses typically occurs after the rainfall event has ended, whereas many studies focus on streamflow changes during the event itself. Additionally, bimodal responses are influenced by catchment-specific topography and geology, making them less observable in certain regions. These challenges highlight the need for more in-depth investigation into bimodal streamflow responses to enhance our understanding of their mechanisms. Therefore, an in-depth investigation into the mechanisms driving these responses is essential. Such research would enable the grouping of similar hydrologic responses and facilitate comparisons of stormflow generation processes across different watersheds (Graham and McDonnell, 2010; Tromp-van Meerveld and McDonnell, 2006a, b).

Extensive studies across diverse regions have explored the role of soil water content and groundwater levels in generating delayed peaks in stormflow. Detty and McGuire (2010) emphasized subsurface flow thresholds in a forested catchment in the USA, while Farrick and Branfireun (2014) analyzed soil moisture and groundwater interactions in Canadian wetlands. Penna et al. (2011) examined antecedent soil moisture and storage thresholds in alpine catchments in New Zealand.

These studies, along with others from regions such as Japan (Haga et al., 2005) and Europe (Graeff et al., 2009), contribute to the growing body of knowledge on threshold behavior in stormflow responses. However, while these studies highlight the occurrence of thresholds, the complex interactions that drive post-threshold runoff processes remain insufficiently understood.

Investigating stormflow events in semi-humid regions, such as XEW, is challenging due to the relatively arid climate and low runoff coefficients. Over nearly a decade, 95 storm events were identified and analyzed in XEW, offering a rare and valuable dataset for examining bimodal stormflow responses in such regions. This study builds on prior findings to uncover the processes underlying delayed stormflow patterns. We hypothesize that the generation of delayed stormflow is governed by threshold-dependent interactions between soil water content (SWC) and groundwater level (GWL). The primary objectives of this study are: (1) to analyze the temporal dynamics of ~~soil water content (~~SWC~~)~~ and ~~groundwater level (~~GWL~~)~~ during storm events, (2) to elucidate the mechanisms driving the threshold behavior observed in bimodal hydrographs, and (3) to reveal the underlying processes responsible for delayed stormflow in XEW.

## 2. Materials and methods

### 2.1 Study site

The study was conducted in the Xitaizi Experimental Watershed (XEW), a 4.22 km² catchment located in North China (40°32′N, 116°37′E), approximately 70 km northeast of Beijing at (Fig. 1). The watershed's elevation ranges from 676 to 1201 m above sea level, and the region experiences a monsoon-influenced semi-humid climate. The average annual precipitation is 625 mm, with 80% concentrated between June and September. The mean annual temperature is 11.5°C with an average relative humidity of 59.1%. Forests cover 98% of the watershed, with broad-leaved species and shrubberies accounting for 54.2% and 33.0%, respectively.

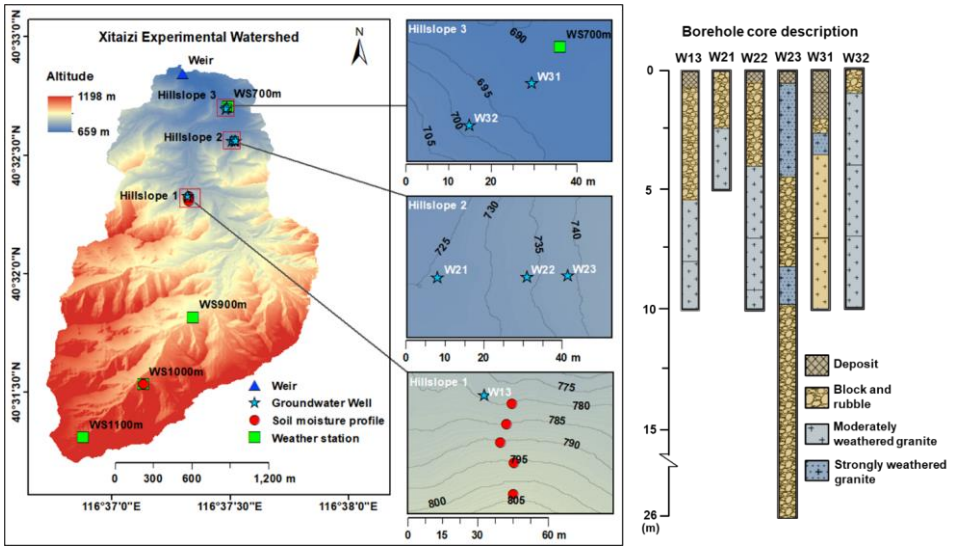


**Figure 1.** Location of Xitaizi Experimental Watershed (XEW) and a simple description of the borehole cores. This figure shows the distribution of monitoring instruments, including four weather stations (WS700, WS900, WS1000, and WS1100), an outlet weir, six groundwater observation wells, and eight soil moisture observation profiles. Of the eight soil moisture profiles, five are located on Hillslope 1, while the remaining three are positioned on the slope near WS1000. Research hillslopes (Hillslope 1, Hillslope 2, and Hillslope 3) are delineated as key zones for hydrological and geological investigations.

The soils in XEW are primarily brown earth and cinnamon soils, with depths up to 1.5 m and an average saturated hydraulic conductivity of 45 mm/h. The surface soil is rich in organic matter, enhancing infiltration and reducing surface runoff potential. Underlying geology is predominantly compacted, deeply weathered granite (80% of the area), with smaller portions of gneiss and dolomite. Fractured granite facilitates vertical and lateral subsurface flow, contributing to delayed groundwater responses. Slug tests estimated the saturated hydraulic conductivity of weathered granite to range from $5.2\times10^{-3}$ m/day to 1.16 m/day.

## 2.2 Research hillslopes and instrumentation

Three research hillslopes (Hillslope 1, Hillslope 2, and Hillslope 3) were selected to investigate hydrological processes under varying geological and topographical conditions. Hillslope 1 (HS1)

features thick soils overlying fractured granite, Hillslope 2 (HS2) has a highly permeable fractured block layer, and Hillslope 3 (HS3) consists of shallow soils over weakly weathered bedrock.

To capture spatial variability, SWC probes and boreholes were installed along hilltops, mid-slopes, and foot slopes. Groundwater boreholes, ranging from 5 to 26 m deep, were equipped with HOBO capacitance water level loggers to record GWLs (Fig. 1).2.3 Meteorological and streamflow data collection

Meteorological data spanning 2013–2023 were collected from four GRWS100 automatic weather stations (WS700, WS900, WS1000, and WS1100), positioned at elevations of 700, 900, 1000, and 1100 m, respectively. Rainfall was recorded at 10-minute intervals using six tipping-bucket rain gauges near the weather stations, and the data were averaged for analysis.

Streamflow was measured at the catchment outlet using a Parshall flume, with water levels logged every 5 minutes since 2014. Data from some events were excluded due to sensor malfunctions or poor data quality, including key rainfall events in 2018 and 2019. Despite these exclusions, 95 rainfall-runoff events were analyzed, offering robust data for investigating bimodal stormflow characteristics.

**2.4 Soil water content and groundwater level monitoring**

Volumetric SWC was monitored at eight sites using CS616 time-domain reflectometry (TDR) probes installed at 10 cm intervals from the surface to 80 cm depth. Five profiles were located along HS1, and three were near WS1000. Measurements were recorded every 10 minutes, and the arithmetic mean of SWC values was used for analysis.

GWLs (below the ground surface, hereinafter referred to as bgs) were observed in six boreholes distributed across the hillslopes. HOBO capacitance water level loggers recorded hourly data. To facilitate comparisons, GWLs were normalized using the method described by Detty and McGuire (2010). This normalization, expressed as the GWL index ($I_G$), standardizes GWLs across wells with varying ranges.

Groundwater levels were normalized following the method described by Detty and McGuire (2010). For each well and event, the median height of the water table above the lowest recordable depth of the instrument was calculated and normalized to the total observed range, where 0 represents the minimum height and 1 represents the maximum height. This normalized value was referred to as the groundwater index ($I_G$). We used $I_G$ to facilitate comparisons across wells with different absolute GWL ranges and to represent the overall GWL dynamics in the watershed.

Streamflow and SWC data were aggregated to hourly intervals for alignment with GWL data. Preliminary analysis confirmed that the delayed second streamflow peak had response times exceeding the hourly scale, rendering this aggregation sufficient for the study's purposes.

### 2.5 Rainfall-runoff event identification and hydrograph analysis

Rainfall events were identified using an intensity-based automatic algorithm described by Tian et al. (2012) that defines event with rainfall intensity >0.1 mm/h and a minimum separation of six hours between events. Events with cumulative rainfall exceeding 5 mm were analyzed.

Bimodal rainfall-runoff events were manually identified based on two criteria: (1) the presence of a secondary, arch-shaped runoff peak occurring after rainfall cessation or during minimal intermittent rainfall, and (2) A distinct separation between the direct (sharp) and delayed (broad) peaks. More details of the classification are described in Cui et al. (2024, HESS).

The combination of automatic event delineation and manual identification ensured the accurate selection of 14 rainfall-runoff events with well-defined delayed peaks for subsequent analysis. Streamflow was separated into storm runoff and baseflow using the HYSEP program with the constant slope method (Hewlett and Hibbert, 1967; Sloto & Crouse, 1996), supplemented by manual adjustments for complex hydrographs. Event stormflow volumes were calculated as total discharge minus baseflow.

Streamflow was separated into storm runoff and baseflow using the HYSEP computer program with the constant slope method, supplemented by manual adjustments for complex hydrographs.

Throughout the manuscript, stormflow refers to the total discharge, and event stormflow volumes were calculated as total discharge minus baseflow, which are expressed in $q_s$.

### 2.6 Hydrological connectivity analysis

Hydrological connectivity among streamflow, SWC, and GWL was analyzed to examine the interplay of subsurface flow pathways. Rainfall-runoff events were analyzed based on their total rainfall (>5 mm) and corresponding streamflow peaks. As illustrated in Fig. 2, The peak rainfall intensity ($R_p$) was determined based on the maximum 1-hour rainfall intensity, with the time of occurrence recorded as $TP_p$. Metrics such as initial streamflow ($Q_0$) and peak streamflow ($Q_p$) were determined alongside their respective timings ($TQ_0$ and $TQ_p$).

Similar metrics were calculated for SWC and GWL, including initial values ($SWC_0$ and $I_{G0}$) and peak values ($SWC_p$ and $I_{Gp}$), with corresponding times of occurrence ($TS_0$, $TI_{G0}$, $TS_p$ and $TI_{Gp}$). These metrics allowed for a comprehensive evaluation of the soil water-groundwater-streamflow response relationship across 95 distinct rainfall-runoff events.

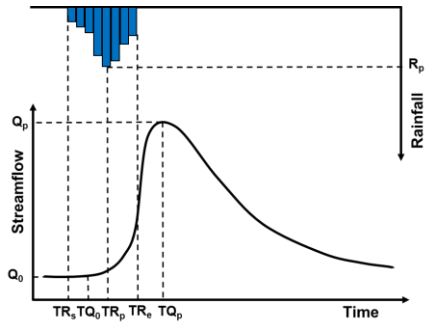


**Figure 2.** Conceptual framework ~~Definition sketch for analysis~~ of rainfall event analysis.

## 3. Results

### 3.1 Hillslope-scale dynamics of SWC and GWL during rainfall-runoff events

The temporal evolution of SWC and GWL was analyzed across 95 rainfall-runoff events to

understand their dynamic interaction. Our analysis revealed a clear relationship between SWC and GWL dynamics, with SWC initially increasing rapidly during rainfall, followed by a stabilization or decline once a threshold was reached. In contrast, GWL showed a more delayed response (Fig. 3). Three distinct patterns of SWC and GWL interaction were identified.

Figure 3 illustrates the dynamics of SWC and GWL during three representative events. These events were selected to demonstrate the variability in SWC and GWL patterns identified across the 95 rainfall-runoff events. The selected events all occurred within the same year to minimize inter-annual variability and ensure comparability. Red circles indicate rainfall periods, while black circles represent post-rainfall periods. In dry conditions, despite 66.6 mm of rainfall, SWC remained relatively low (<0.20), with a gradual increase during rainfall followed by stabilization after rainfall ceased. GWL showed minimal response. (Fig. 3a).

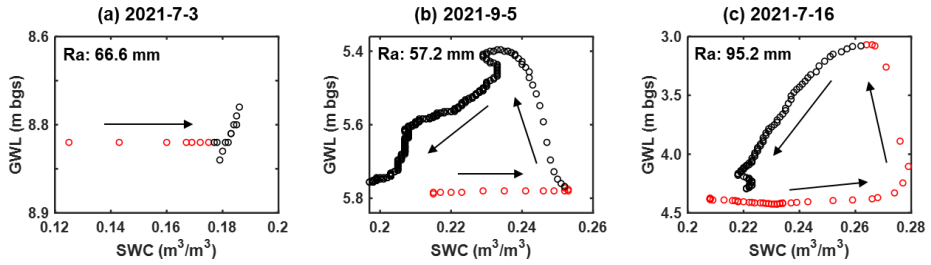


**Figure 3.** Three typical SWC-GWL dynamics patterns during rainfall-runoff events. Ra is rainfall amount. Arrows indicate the temporal evolution of the events. Red circles indicate periods of rainfall, while black circles denote post-rainfall periods.

In events with wet conditions, both SWC and GWL showed significant increases. However, the timing of GWL rise varied: in some cases, GWL rose after the cessation of rainfall, while in other cases, it began rising before the rainfall ended. The primary distinction between these patterns lies in the timing of the GWL rise: in Fig. 3b (57.2 mm rainfall), GWL began to rise after the rainfall ended, whereas in Fig.3c (95.2 mm rainfall), GWL started to rise noticeably before the end of the rainfall.

In the ~~scenario~~ case represented by Fig. 3b, SWC increased significantly, surpassing 0.20, while GWL showed a delayed rise after the rainfall ceased. The counterclockwise hysteresis was observed

as SWC continued to increase while GWL remained largely unchanged during rainfall. Fig. 3c, which typically represents intense storm events, showed a sharp increase in both SWC and GWL, with SWC exceeding 0.25. GWL began to rise before the rainfall ended, reaching a peak as rainfall continued, and both variables showed a substantial decline after rainfall ceased. These representative events highlight the variability in the SWC-GWL relationship, with timing differences in the rise of GWL and distinct hysteresis patterns during moderate and extreme events.

We further quantified the frequency distribution of SWC and GWL increases or decreases across the 95 rainfall-runoff events (Fig. 4). Notably, in 49 events, SWC increased, while GWL increased in 43 events. In contrast, SWC declined in 26 events and GWL declined in 15 events. Importantly, 15 events showed a simultaneous decline in both SWC and GWL, which were associated with delayed stormflow and larger stormflow volumes. One such event, on August 15, 2021, exhibited fluctuating SWC and GWL values throughout the rainfall event due to the more dispersed rainfall distribution. As a result, our subsequent analysis primarily focused on the remaining 14 events with well-defined response characteristics.

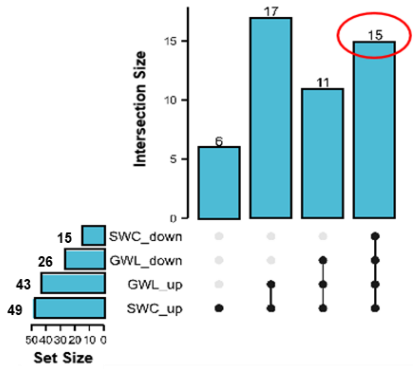


**Figure 4**. ~~Upset~~ UpSet plot of the response characteristics of SWC and GWL during rainfall-runoff events.

### 3.2 SWC dynamics across rainfall-runoff events

Figure 5 presents the SWC dynamics observed during 14 distinct rainfall-runoff events, each

characterized by minimal or no intermittent rainfall during the recession period. To facilitate a clear comparison of SWC changes across events, the peak of each event was aligned with a horizontal axis value of 0.

During the initial rainfall phase, SWC increased rapidly, reaching a peak value. As the rainfall ceased, SWC began to decline, though at a slower rate, eventually stabilizing at a specific value. To quantify the threshold at which SWC stabilizes, we conducted a statistical analysis of the stable SWC during these events. The stable phase was defined as the period following the recession phase when SWC exhibited minimal variation before subsequent rainfall. The statistical analysis of the stable SWC revealed a mean value of 0.1974, with a standard deviation of 0.0158 and a 95% confidence interval of [0.1945, 0.2003]. These results validate the visually observed threshold of 0.20 for SWC stabilization. The general pattern of SWC variation is schematically illustrated in Fig. 6.

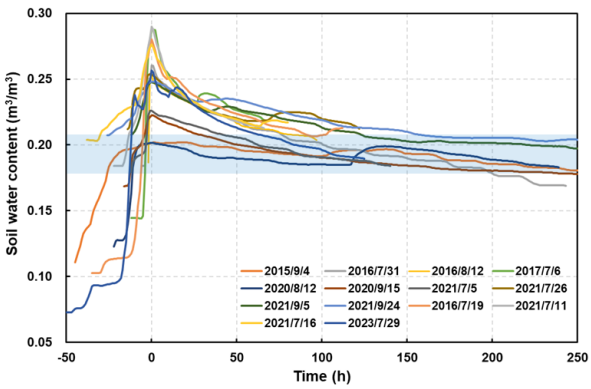


**Figure 5.** SWC dynamics during different storm events.

The SWC response to rainfall is rapid. Upon rainfall onset, SWC increased sharply. Once the rainfall ceased, the subsequent behavior of SWC depends on whether the peak value exceeds the 0.20 threshold. If SWC remains below or at 0.20, it either stabilizes or declines slowly. However, when SWC exceeds 0.20, it decreased rapidly before stabilizing around the 0.20 threshold. The magnitude of the peak above 0.20 influences the speed of the subsequent decline in SWC: the greater the peak, the faster the decline.

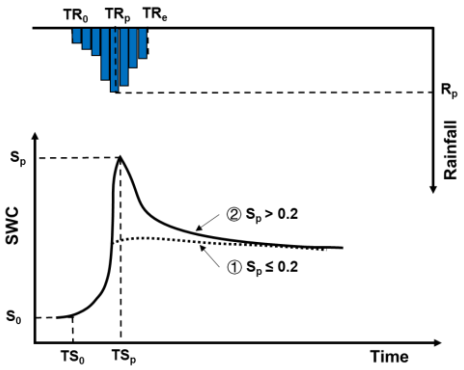


**Figure 6.** Conceptual~~Schematic~~ diagram of SWC response during storm events. $S_p$ is the maximum SWC value.

### 3.3 GWL dynamics and response types

This section examines GWL dynamics during 14 selected rainfall-runoff events, chosen for their clear and consistent GWL and SWC patterns. These events facilitate a detailed investigation into groundwater response to storm events. Two distinct GWL response types—quick and slow—were identified and are conceptually illustrated in Fig. 7. It is important to note that Fig. 7 is a conceptual~~schematic~~ representation, not based on specific rainfall-runoff events, and does not include rainfall depth data.

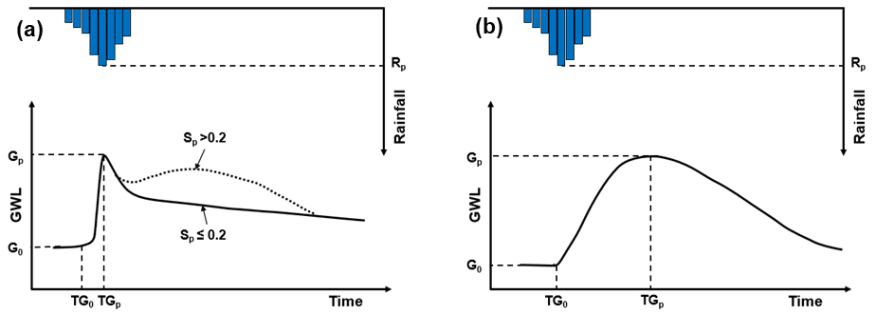

**Figure 7.** Conceptual~~Schematic~~ diagram of GWL response during storm events. $G_0$ and $G_p$ represent the initial and maximum values of GWL, respectively. $S_p$ denotes the maximum SWC value.

In events exhibiting a quick response, the GWL rises rapidly, closely aligning with the SWC peak. The GWL response typically lags behind the SWC peak by 0 to 6 hours (Fig. 7a). For events where SWC exceeds 0.20 (and particularly when it surpasses 0.24), the GWL often shows a secondary rise following the initial peak, as indicated by the dotted line in Fig. 7a. Conversely, the slow response occurs when SWC declines sharply after reaching its peak, resulting in a delayed rise in GWL (Fig. 7b).

An analysis of GWL responses across various hillslopes revealed spatial variability. For instance, the GWL at HS2 (well W21-23) exhibited a quick response (Fig. 7a), whereas GWLs at HS1 (W13) and HS3 (W31 and W32) displayed slow response characteristics (Fig. 7b). These findings suggest that the GWL dynamics are influenced not only by SWC but also by the underlying geological structure of each hillslope.

At the watershed scale, GWL response to storm events demonstrated considerable spatial variability. $I_G$, represents the average normalized GWL across multiple wells, was used to capture an integrated view. Analysis revealed that $I_G$ often exhibited two distinct peaks during storm events. Among the 14 events analyzed, 9 events displayed dual $I_G$ peaks, coinciding with the two peaks in streamflow. However, at the individual well level, only W13 (HS1) and W23 (HS2) exhibited dual GWL peaks. Specifically, W13 showed two peaks during one event, while W23 exhibited two peaks during five events. The remaining wells displayed only a single peak across all events analyzed (see Table 1).

**Table 1.** Statistical results of response characterization of streamflow, $I_G$ and groundwater levels.

| | | | **HS1** | | **HS2** | | **HS3** | |
|---|---|---|---|---|---|---|---|---|
| | **Streamflow** | $I_G$ | **W13** | **W21** | **W22** | **W23** | **W31** | **W32** |
| Total number of events | 14 | 14 | 14 | 8 | 14 | 14 | 9 | 9 |

| | | | | | | | | |
|---|---|---|---|---|---|---|---|---|
| Number of events with two peaks | 9 | 9 | 1 | 0 | 0 | 5 | 0 | 0 |

### 3.4 GWL responses across hillslope positions

Further examination of GWL responses across various locations is presented in Fig. 8, which shows the magnitude of GWL increases and their lag times relative to rainfall onset. While variations in GWL were observed among the monitoring wells, the differences in GWL increments were generally modest, with mean increases ranging from 1 to 2 meters. Notably, smaller GWL changes were recorded at the foot of the hillslope (e.g., W21 and W31). Within the same hillslope, GWL increments tended to increase progressively from the foot to the top, as seen in HS2 (W21-W23) and HS3 (W31 and W32).

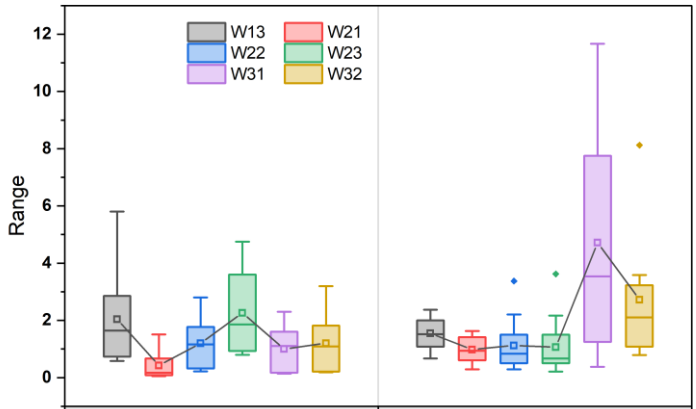


| | △GWL (m) | | | | | | Lag time (day) | | | | | |
|---|---|---|---|---|---|---|---|---|---|---|---|---|
| Location | W13 | W21 | W22 | W23 | W31 | W32 | W13 | W21 | W22 | W23 | W31 | W32 |
| Min | 0.6 | 0.1 | 0.2 | 0.8 | 0.1 | 0.2 | 0.7 | 0.3 | | 0.2 | 0.4 | 0.8 |
| Max | 5.8 | 1.5 | 2.8 | 4.8 | 2.3 | 3.2 | 2.4 | 1.6 | 3.4 | 3.6 | 11.7 | 8.1 |
| Mean | 2.0 | 0.4 | 1.2 | 2.3 | 1.0 | 1.2 | 1.5 | 1.0 | 1.1 | | 4.7 | 2.7 |

**Figure 8.** GWL increments (ΔGWL) and lag time of peak GWL relative to rainfall onset at different locations.

In contrast, the lag times for maximum GWL exhibited greater variation across locations. For instance, at HS3, lag times ranged from 0.4 to 11.7 days at W31 and from 0.8 to 8.1 days at W32, significantly longer than those at HS1 (0.7 to 2.4 days) and HS2 (0.2 to 3.6 days). Interestingly, within

a single hillslope, no consistent relationship was found between the lag time of maximum GWL and its distance from the foot of the hillslope.

To further investigate these dynamics, the relationship between GWL increments and SWC was analyzed across 14 storm events (Fig. 9). The analysis focused on six observation wells (W13, W21–W23, W31, and W32) located on three hillslopes (see Fig. 1 for well locations). The variability in GWL response types—quick versus slow—was attributed to spatial differences in SWC thresholds and hillslope geological structures.

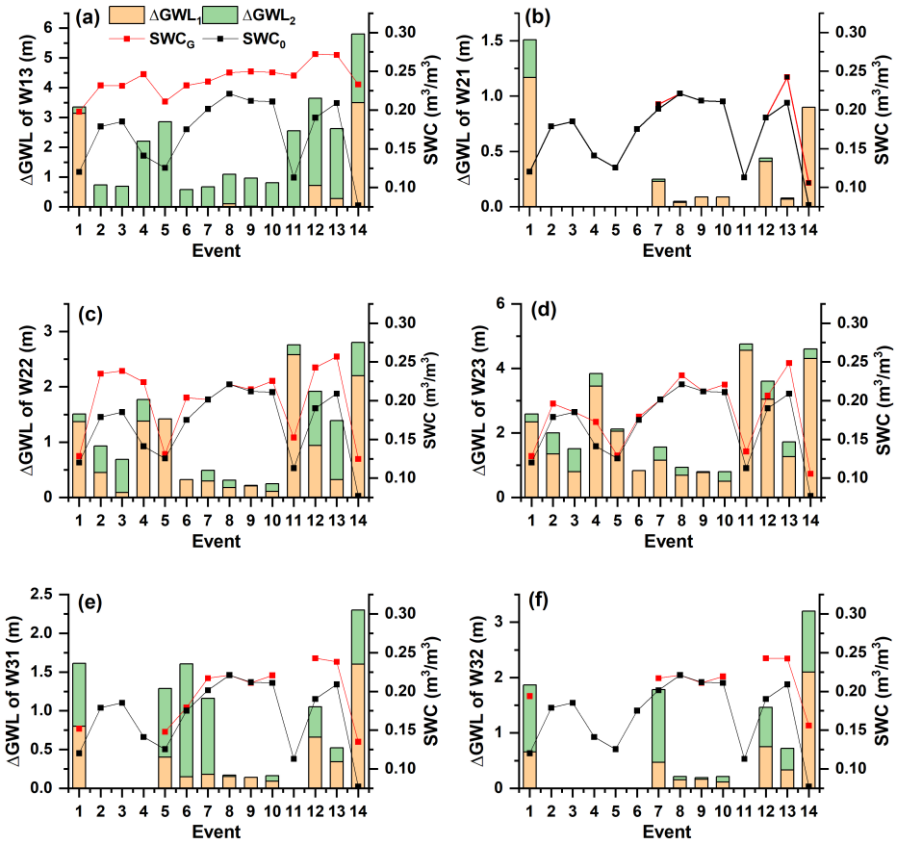

**Figure 9.** GWL increments (ΔGWL) across various locations during 14 storm events, along with initial SWC ($SWC_0$) and SWC at the onset of GWL rise ($SWC_G$). The orange bars represent ΔGWL during the SWC increase phase, while the green bars represent ΔGWL during the SWC decline phase. The red and black lines denote $SWC_G$ and $SWC_0$, respectively.

In Fig. 9, the orange bars represent GWL increments during the SWC increase phase (up to its peak), while the green bars indicate GWL increments during the SWC decline phase (from its peak to when GWL reached its maximum. The black and red dotted lines mark the initial SWC ($SWC_0$) and the SWC at the onset of GWL rise ($SWC_G$), respectively. Missing data for some locations are indicated by the absence of bars in Figs. 9b, 9e, and 9f.

The analysis revealed that the magnitude of the SWC increase following rainfall onset is a key determinant of delayed GWL responses. Specifically, a greater difference between $SWC_G$ and $SWC_0$ corresponded to an onset of GWL rise begins. Conversely, when $SWC_G$ and $SWC_0$ are similar, GWL rose almost simultaneously with the SWC increase.

At HS1 (W13), GWL began to rise only after SWC exceeded 0.20. Most of the GWL increase occurred during the SWC decline phase, suggesting that soil wetness exerts a threshold effect on GWL dynamics. This delayed response aligns with the slow response type. At HS2 (W21-23), GWL responses were more immediate, with GWL increases closely following SWC rises. $SWC_G$ values at these locations ranged widely (0.13-0.26) but were generally close to $SWC_0$, indicating that GWL responses at HS2 are less dependent on SWC thresholds and exhibit a quick response type.

HS3 demonstrated both quick and slow GWL responses. Initial rises occurred soon after the SWC increase, but the majority of GWL increments took place during the prolonged SWC decline phase following its peak. This pattern suggests a more complex interaction of immediate and delayed factors influencing GWL dynamics at HS3.

These findings highlight a strong relationship between the emergence of quick and slow GWL response types and SWC dynamics. In quick response types, GWL increments occur primarily during the SWC increase phase, resulting in a steep response curve. In slow responses, GWL increments predominantly occur during the SWC decline phase, producing an arch-shaped response curve. These

distinctions underscore the pivotal role of SWC dynamics in regulating the timing and magnitude of GWL responses across different hillslopes.

### 3.5 Characterization of groundwater response at the watershed scale

Figure 10 illustrates the timing of $I_G$ peaks relative to SWC response. The first $I_G$ peak occurred rapidly following rainfall, initiating 0-2 h after the SWC began to rise and reaching its peak occurring 0-9 h later (mean: 3.7 h) after SWC reached its maximum. In contrast, the second $I_G$ peak typically occurred post-rainfall, lagging behind the SWC peak by 10-65 h (mean: 28 h). These patterns align with the quick and slow GWL response types identified in section 3.2. The occurrence of dual $I_G$ peaks can be attributed to the superimposition of groundwater contributions from different hillslopes with differing response rates. The first (quick) GWL response is tightly coupled to rainfall onset and SWC increases, while the second (slow) GWL response reflects gradual infiltration and groundwater recharge occurring over a broader timescale.

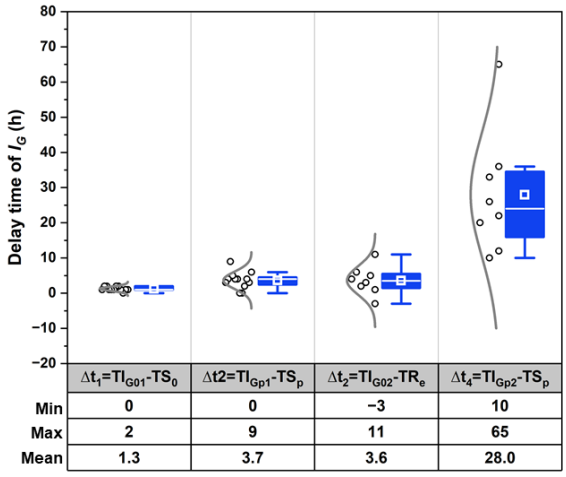


| | $\Delta t_1$=$TI_{G01}$-$TS_0$ | $\Delta t2$=$TI_{Gp1}$-$TS_p$ | $\Delta t_2$=$TI_{G02}$-$TR_e$ | $\Delta t_4$=$TI_{Gp2}$-$TS_p$ |
|---|---|---|---|---|
| Min | 0 | 0 | −3 | 10 |
| Max | 2 | 9 | 11 | 65 |
| Mean | 1.3 | 3.7 | 3.6 | 28.0 |

**Figure 10.** Delay time of $I_G$ peaks relative to peak SWC. $TI_{G01}$ and $TI_{G02}$ represent the onset times of the first and second peaks of $I_G$, respectively. $TS_0$ and $TS_p$ indicate the time when SWC started to increase and peaked, respectively. $TI_{Gp1}$ and $TI_{Gp2}$ represent the time when $I_G$ started to increase and peaked, respectively. $TR_e$ indicates the end of rainfall.

The growth rates of $I_G$ towards the two peaks were also quantified (Fig. 11). A notable disparity was observed between the growth rates of the first ($r_1$) and second ($r_2$) $I_G$ peaks. The first $I_G$ peak exhibited a markedly faster rates (0.03 to 0.98/day, mean: 0.38/day) compared to the second peak (0.01 to 0.31/day, mean: 0.07/day). These differences reflect the contrasting dynamics of quick and slow GWL responses across hillslopes. In events featuring dual $I_G$ peaks, the maximum $I_G$ was typically observed at the second peak. However, in events with higher GWLs (indicating lower $I_G$), the disparity between the growth rates diminished, making the two peaks harder to distinguish (e.g., Events 9 and 10). In Events 11-14, where GWLs were significantly higher, only a single $I_G$ peak was observed.

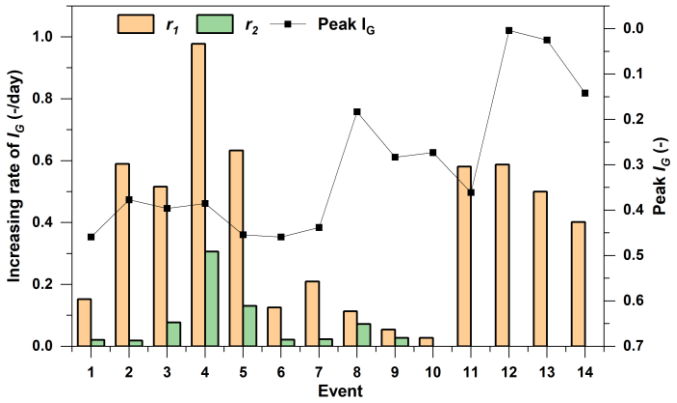


**Figure 11.** Growth rates of $I_G$ and the maximum $I_G$ value across storm events. $r_1$ and $r_2$ denote the ascent rates during the first and second peaks, respectively.

The contrasting dynamics of the two $I_G$ peaks highlight their distinct formation mechanisms. The first $I_G$ peak, occurring during rainfall, is closely associated with the rapid rise in SWC. Conversely, the second $I_G$ peak emerges post-rainfall, coinciding with soil draining and groundwater recharge processes. As reported by Dang et al. (2023), rainfall induces pressure waves that rapidly

expel soil water from the lower soil column, while infiltrated rainwater migrates downwards at slower pace. pressure-driven displacement generates a near-instantaneous GWL response during the initial phase of rainfall.

We conjecture~~hypothesize~~ that the rapid $I_G$ peak is linked to kinematic wave triggered by increased SWC, which displaces pre-existing "old" soil water and groundwater, leading to a synchronized GWL rise (e.g., Anderson and Burt, 1978). Despite the slow percolation of water through soil and bedrock, the theoretical celerity of this kinematic response is near-instantaneous, accounting for the rapid GWL rise. Furthermore, drilling data suggest that the presence of faults in the bedrock of HS2, potentially facilitating faster groundwater response on this hillslope compared to others.

The second, slow $I_G$ peak is likely driven by the gradual infiltration of rainwater into deeper soil and bedrock layers, ultimately recharging the groundwater. This process is regulated by the soil's water storage threshold. Before reaching this threshold, the soil retains all incoming rainfall. Once exceeded, excess water drains rapidly into deeper layers, leading to a decline in SWC and a concurrent rise in GWL due to groundwater recharge.

# 4. Discussion

## 4.1 Inter-hillslope GWL dynamics

GWL variations in lag times and response magnitudes across hillslopes can be attributed to differences in geological conditions. HS1 and HS3 are primarily underlain by fully to strongly weathered granite, with upper layers comprising significant soil-rock mixtures. These features lead to relatively slower GWL responses, likely due to the limited permeability of the regolith and underlying materials. In contrast, HS2 is characterized by a fractured rock layer at depths of 10-30 meters (see Fig. 1), which enhances subsurface flow and facilitates faster GWL responses. These geological contrasts explain the observed differences in GWL response times among the hillslopes.

Among the three hillslopes, HS3 exhibited the slowest GWL responses, characterized by the

longest lag times. This distinct behavior makes HS3 a crucial reference for understanding inter-hillslope variations in GWL dynamics. Previous study by Cui et al. (2024) highlighted that GWL response times are closely linked to delayed stormflow timing, emphasizing the importance of examining GWL dynamics. Comparing the GWL response times of HS1 and HS2 with those of HS3 provides insights into how geological structures and SWC thresholds influence delayed stormflow generation.

Furthermore, the deeply weathered regolith and extensive fracturing in HS2 promote more rapid stormflow generation, as water stored in the regolith layer contributes to streamflow over extended periods. This finding aligns with previous studies (Kosugi et al., 2011; Padilla et al., 2015), which demonstrated that geological features such as fracture density and weathering depth influence subsurface flow paths and, ultimately, groundwater dynamics.

To deepen understanding of the inter-hillslope differences in GWL responses, we calculated the lag times between rainfall onset and peak GWL responses for all observation wells on each hillslope, incorporating spatial variability. Average lag times, denoted as $t_{S1}$, $t_{S2}$ and $t_{S3}$ for HS1, HS2, and HS3, respectively, were used to calculate the time differences $\Delta t = t_{S1} - t_{S3}$ and $\Delta t = t_{S2} - t_{S3}$. These time differences were then analyzed for their correlation with $I_G$, as illustrated in Fig. 12.

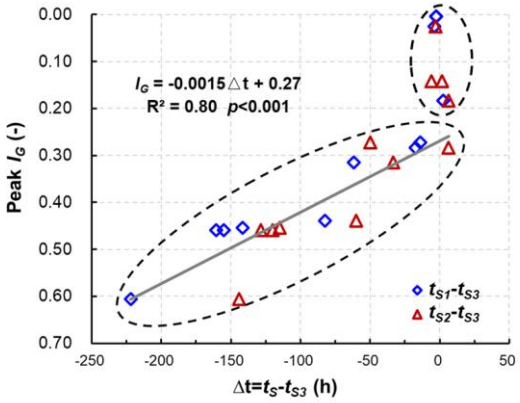

**Figure 12.** Correlation between peak $I_G$ and the time differences from peak GWL responses on HS1, and HS2 to HS3 ($\Delta t = t_{S} - t_{S3}$), where $t_{S1}$, $t_{S2}$ and $t_{S3}$ are the average lag times of peak GWLs on HS1, HS2 and HS3, respectively.

In Fig. 12, blue diamonds represent $\Delta t = t_{S1} - t_{S3}$, while red triangles represent $\Delta t = t_{S2} - t_{S3}$. Both pairs exhibit a significant negative correlation with peak $I_G$, described by the equation: $I_G = -0.0015 \times \Delta t + 0.27$ ($R^2 = 0.80$, $p < 0.001$). These results indicate that higher $I_G$ values correspond to shorter inter-hillslope lag times, suggesting enhanced hydrological connectivity and transmissivity feedback mechanisms, as described in previous studies (Kendall et al., 1999; Bishop et al., 2011).

As peak $I_G$ approaches 0.30, $\Delta t$ converges to near-zero with minimal fluctuations, particularly during extreme storm events. This finding supports the results presented in Fig. 11, which demonstrate that elevated GWLs synchronize GWL responses across the watershed. This synchronization reflects a critical hydrological mechanism driven by transmissivity feedback, which amplifies groundwater movement, reduces lag times, and enhances watershed-scale connectivity. This dynamic is consistent with the work of Padilla et al. (2015), who reported that shorter lag times in bedrock aquifers with high-transmissivity conduits, and Scaife et al. (2020), who noted that increased connectivity during high GWL conditions reduces lag times and enhances watershed-scale hydrological responses.

Furthermore, although Fig. 12 labels the vertical axis as $I_G$ to represent watershed-wide GWL status, a similar pattern emerges when replacing $I_G$ with site specific GWL values, though the GWL thresholds may vary among observation sites. These observations reinforce the idea that watershed-scale groundwater dynamics are influenced by the interplay between spatially variable geological conditions and temporal variations in GWL.

### 4.2 Delayed stormflow processes linked to GWL dynamics

Previous studies have shown that streamflow in XEW frequently exhibits a bimodal hydrograph during heavy rainfall, with delayed stormflow likely originating from shallow groundwater outflow (Cui et al., 2024). Understanding the timing and lag between groundwater and streamflow responses is crucial for identifying dominant runoff generation mechanisms (Beiter et al., 2020). Discrepancies

in these timings can indicate contributions from different water sources to the stream channel. Fig. 13 illustrates the relative timing of maximum $I_G$ ($I_{Gp}$) and maximum SWC ($SWC_p$) for eight storm events, alongside rainfall duration.

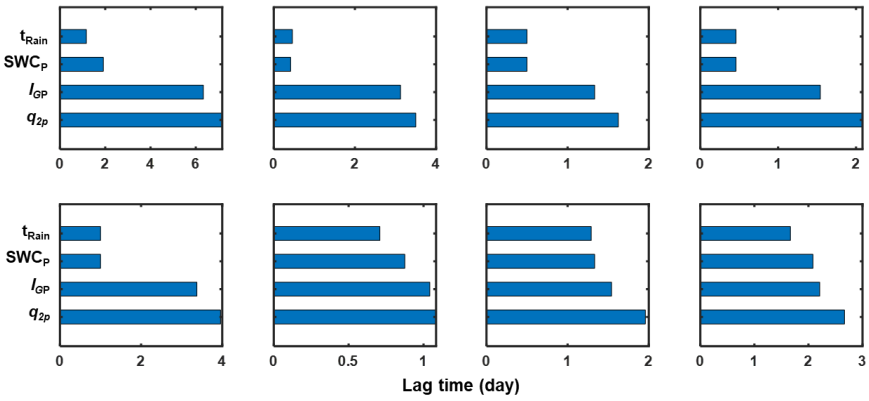


**Figure 13.** Lag times of maximum SWC and GWL relative to rainfall onset. Each bar indicates the rise and peak times of the corresponding variable, with $t_{Rain}$ indicating rainfall duration. $SWC_{SP}$ and $I_{GP}$ represent the maximum SWC and $I_G$, respectively, while $q_{2p}$ denotes the delayed streamflow peak.

Rainfall durations for the analyzed events ranged from 0.46 to 1.67 days. SWC, $I_G$, and delayed stormflow ($q_{2p}$) followed a clear sequence in their peak timings relative to rainfall onset. SWC responded rapidly, with its peak occurring 0.4 to 2.1 days after rainfall began, usually coinciding with or slightly after rainfall cessation. In contrast, $I_G$ continued to increase after the SWC peak and reached its maximum before the delayed stormflow peak ($q_{2p}$). While the lag times between $SWC_p$, $I_{Gp}$, and $q_{2p}$ varied among events, the lag between $I_{Gp}$ and $q_{2p}$ remained relatively consistent.

This pattern aligns with findings from Haught and Meerveld (2011) and Rinderer et al. (2016), who suggest that when groundwater response precedes or synchronizes with streamflow, it indicates strong hillslope-stream connectivity, with groundwater serving as the primary driver of streamflow. Our results corroborate this view, showing that $q_{2p}$ timing is predominantly governed by groundwater dynamics. This relationship is further validated by the strong linear correlation between the lag times

of $q_{2p}$ ($t_{2p}$) and $I_{Gp}$ ($t_{IGp}$), as indicated by the regression equation $t_{2p} = 1.11\times t_{IGp} + 0.17$, with a slope of 1.11, showing a high determination coefficient ($R^2 = 0.995$, $p < 0.01$). (Fig. 14).

Conversely, the correlation between $t_{2p}$ and the lag time of $SWC_p$ ($t_{SWCp}$) was weak ($R^2 = 0.029$, $p = 0.688$), indicating that the timing of $SWC_p$ has minimal influence on the delayed streamflow peak. Additionally, the $I_G$ pattern during the delayed stormflow period closely mirrored the shape of the streamflow hydrograph (Fig. A1), reinforcing the dominant role of $I_G$ plays in controlling delayed stormflow.

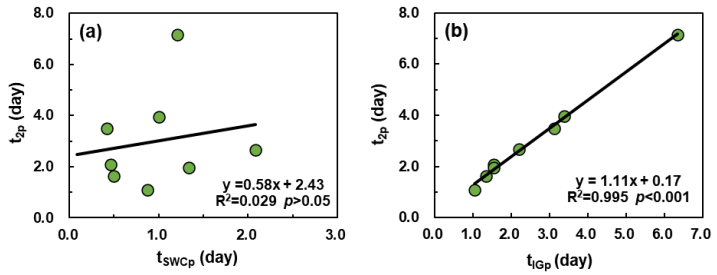


**Figure 14.** Lag times of maximum (a) SWC and (b) $I_G$ relative to delayed streamflow peaks ($t_{2p}$). $t_{SWCp}$ and $t_{IGp}$ denote the peak times of the SWC and $I_G$, respectively.

Further quantitative analysis revealed a strong exponential relationship between streamflow and $I_G$ during the delayed stormflow period (Fig. 15). In the non-rainfall phase of the eight bimodal events, streamflow increased exponentially with GWL ($IG_p$), exhibiting a highly significant correlation ($p < 0.001$) and a determination coefficient of $R^2 = 0.90$. This exponential increase in streamflow is attributed to the increase in lateral hydraulic conductivity as the water table approaches the surface. Similar findings have been reported by Detty and McGuire (2010) and Kendall et al. (1999), where groundwater outflow dominates during storm events.

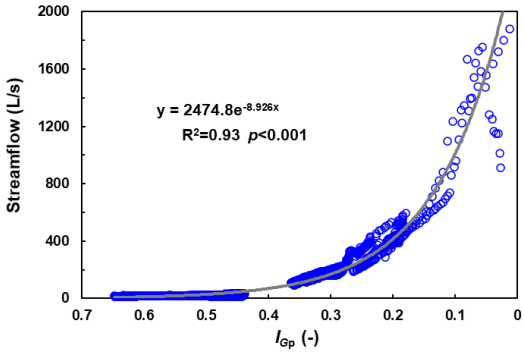


485

486 **Figure 15.** Correlation between $I_G$ and streamflow during delayed stormflow periods.

487 At higher GWLs, the curve of GWL vs. streamflow begins to flatten, suggesting a feedback
488 mechanism. As the rising water table mobilizes shallow groundwater outflow, water is rapidly
489 transported to the stream via shallow flow paths. This process, often referred to as transmissivity
490 feedback, is consistent with Lundin's (1982) description of groundwater dynamics during delayed
491 stormflow periods.

492 **4.3 Delayed stormflow processes linked to GWL dynamics**

493 Understanding the critical thresholds that govern the movement of water within landscapes is
494 essential for accurately predicting delayed stormflow, as emphasized by McDonnell et al. (2021).
495 This study identified a strong Relationship between delayed stormflow and the gradual response of
496 GWL, primarily influenced by a sharp decline in SWC when it exceeds a critical threshold of 0.20.

497 To identify the threshold for delayed stormflow initiation in XEW, we analyzed 63 out of 95
498 rainfall-runoff events with complete streamflow data. The relationship between SWCp and $q_s$ for
499 these events is illustrated in Fig. 16. A clear threshold behavior emerged: when SWC was below 0.20,
500 $q_s$ remained minimal consistent with unimodal events. However, as SWC exceeded 0.20, a noticeable
501 increase in $q_s$ was observed, signaling the onset of delayed stormflow in some events. Specifically,
502 when SWC surpassed 0.23, a pronounced surge in stormflow volume occurred, accompanied by the
503 emergence of a secondary stormflow peak in all events. These findings suggest that the critical

threshold for delayed stormflow initiation lies within the SWC range of 0.20 to 0.23.

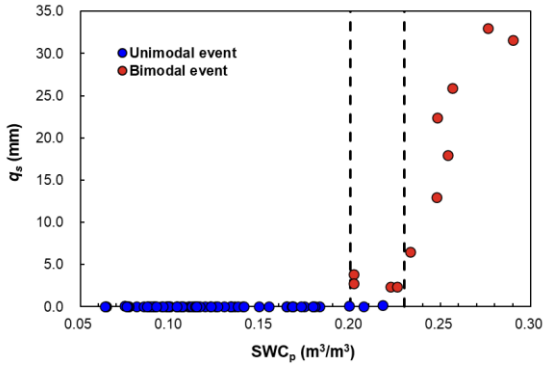


**Figure 16.** Relationship between maximum SWC ($SWC_p$) and event stormflow volume ($q_s$).

These results underscore the pivotal role of the surface soil layer's water deficit or water-holding capacity in triggering delayed stormflow. During rainfall events, the soil retains water until its water-holding capacity is exceeded. Once SWC surpasses the threshold of 0.20, the soil begins to release water more rapidly, initiating delayed stormflow. Additionally, during unimodal events, stormflow ($q_s$) remained consistently below 1 mm despite variations in SWC, indicating that stormflow in these cases arises mainly from direct rainfall interception by the channel rather than delayed soil water release.

While the depth and distribution of soil layers likely influence the watershed's overall water storage capacity, observed SWC data showed minimal spatial variability across locations within the watershed. This suggests that SWC can reliably represent the watershed's overall soil water storage capacity.

One limitation of this study lies in the indirect estimation of field capacity through observed SWC thresholds rather than direct measurement or modeling. Although this approach aligns with observed patterns and simplifies the analysis, it does not fully capture the spatial variability of field capacity or its dependence on soil depth. Future work should incorporate direct field capacity

measurements or modeling to refine the relationship between SWC and delayed stormflow initiation, thereby improving the accuracy of threshold predictions.

### 4.4 Conceptual model of runoff generation in XEW

This section presents a conceptual model elucidating the runoff generation mechanisms in XEW, with a particular focus on the interplay between soil water storage and GWL dynamics. Soil water storage is identified as the critical factor driving the transition from initial to delayed runoff generation. Once the soil water deficit is replenished, the slowly rising GWL becomes the dominant control in the delayed stormflow process. Fig 17 illustrates the conceptual framework, which incorporates transmissivity feedback mechanisms to explain the formation of distinct hydrograph patterns.

**~~1.~~a) Runoff generation under dry conditions (Fig. 17b):**

带格式的: 编号 + 级别: 1 + 编号样式: a, b, c, … + 起始编号: 1 + 对齐方式: 左侧 + 对齐位置: 0.85 厘米 + 缩进位置: 1.48 厘米

In dry watershed conditions, characterized by low antecedent moisture and light rainfall, rainwater primarily infiltrates and is retained in the soil profiles. Streamflow during such events consists of two primary components: (1) a rapid yet modest streamflow peak driven by direct rainfall onto the channel and (2) a relatively stable baseflow originating from the gradual release of deep groundwater reservoirs.

Under these conditions, the baseflow reflects the slow release of groundwater stored in deeper aquifers, while the limited rainfall input is insufficient to trigger significant connectivity between hillslopes and the channel.

**~~2.~~b) Delayed stormflow during moderate storms (Fig. 17c):**

带格式的: 编号 + 级别: 1 + 编号样式: a, b, c, … + 起始编号: 1 + 对齐方式: 左侧 + 对齐位置: 0.85 厘米 + 缩进位置: 1.48 厘米

As rainfall intensity and duration increase, moderate storm events lead to the replenishment of soil water deficits, resulting in the exceedance of soil storage capacity. Initially, the response resembles that of dry conditions, with a rapid streamflow peak generated by direct channel rainfall. However, as rainfall continues, excess water infiltrates deeper, elevating the GWL and expanding the saturated zone.

This process enhances the hydraulic connectivity between the stream channel and adjacent hillslopes, facilitating the lateral transport of shallow groundwater to the channel. As the GWL intersects more conductive soil layers, a delayed stormflow peak is observed, typically occurring after rainfall ceases. This secondary peak reflects the combined effects of deep infiltration, gradual GWL rise, and increased transmissivity in the subsurface, which accelerates shallow groundwater movement towards the channel.

**~~3.~~c) Runoff generation during extreme storm events (Fig. 17d):**

Extreme storm events, characterized by high rainfall intensity and large volumes, result in a sharp and widespread rise in GWL across the entire watershed. During such events, the rapid expansion of saturated areas and the increased hydraulic conductivity of the subsurface enable the swift mobilization of shallow groundwater. This synchronous response generates a pronounced flood peak within a short timeframe.

In the riparian zones, GWLs may rise into the soil profile or even reach the ground surface, facilitating direct water flow into the channel via subsurface pathways. Observational data from extreme events corroborate this mechanism, as significant increases in SWC are recorded in the deeper soil layers of riparian zones after rainfall ends. This pattern suggests that groundwater from adjacent hillslopes contributes to the replenishment of soil water in these zones, reinforcing lateral subsurface flow pathways.

带格式的: 编号 + 级别: 1 + 编号样式: a, b, c, … + 起始编号: 1 + 对齐方式: 左侧 + 对齐位置: 0.85 厘米 + 缩进位置: 1.48 厘米

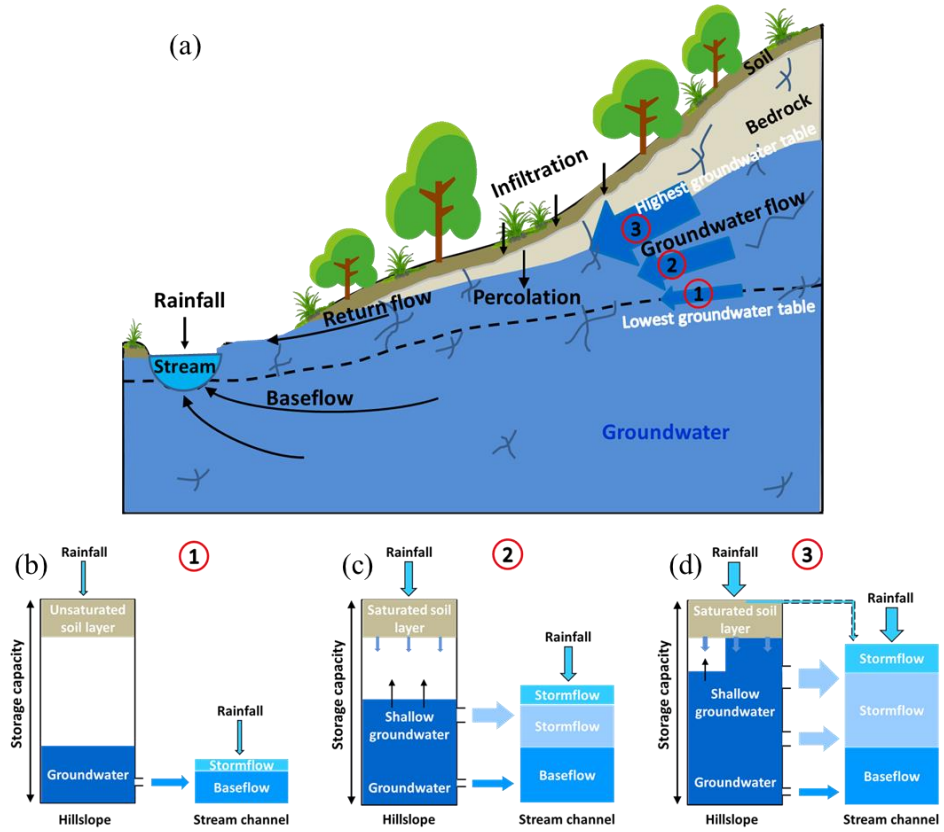


564

565 **Figure 17.** Conceptual model illustrating stormflow generation associated with the transmissivity
566 feedback.

567 The progression from the runoff generation under dry conditions (Fig. 17b) to moderate storm
568 scenarios (Fig. 17c) and ultimately extreme events (Fig. 17d) reflects the progressive wetting-up of
569 the watershed. Abrupt changes in stormflow volume and timing are initially governed by soil water
570 storage thresholds and subsequently controlled by the hydraulic conductivity of the bedrock and
571 micro-topography.

572 This conceptual model provides a quantitative framework for understanding how variations in
573 hydrological conditions influence runoff generation processes in XEW. By integrating soil water

storage dynamics, GWL responses, and transmissivity feedback mechanisms, the model offers insights into the nonlinear behavior of runoff processes under different rainfall scenarios.

## 5. Conclusions

Building upon previous work that identified and characterized bimodal streamflow patterns in XEW, this study quantitatively analyzed SWC and GWL dynamics at the event scale to elucidate the mechanisms driving delayed stormflow generation. The findings reveal that when soil water storage surpasses its holding capacity, a secondary increase in streamflow is triggered. This secondary, or delayed, stormflow is primarily governed by GWL dynamics, which dictate both the magnitude of the delayed response and the lag time to its peak.

During rainfall events, SWC responds rapidly, increasing until the soil's water storage capacity is reached or exceeded. If the stored water remains within this capacity, SWC stabilizes or decreases gradually following the cessation of rainfall, eventually leveling off near the field capacity. The rate of this decrease is closely linked to the extent of SWC exceeding the field capacity. When SWC begins to decline, excess rainwater percolates deeper into the soil, raising the GWL. Once GWL begins to rise, it becomes the dominant driver of the delayed stormflow process.

As GWL rises, hydraulic conductivity increases, facilitating enhanced groundwater flux from hillslopes to the stream channel. This process expands the effective connectivity between the channel and adjacent hillslopes. At specific high GWL thresholds, the synchronization of GWL responses across multiple hillslopes significantly amplifies stormflow volume. This synchronized response shortens the lag time and increases the volume of delayed stormflow, often merging the delayed peak with the direct stormflow peak.

These findings offer critical insights into the nonlinear processes governing stormflow generation and the formation of bimodal hydrographs. By elucidating the mechanisms underpinning these dynamics, the study advances hydrological theory and provides actionable knowledge for improving flood modeling and prediction.

## Data availability

The data supporting this study are available on the Zenodo website at https://doi.org/10.5281/zenodo.12581739.

## Author contribution

ZC contributed the conceptualization, formal analysis, investigation and writing; FT contributed the conceptualization, formal analysis and revision.

## Competing interests

Fuqiang Tian is a member of the editorial board of Hydrology and Earth System Sciences.

## Acknowledgements

This study was supported by National Key R&D Program of China (2022YFC3002902) and National Natural Science Foundation of China (51825902).

## 5. References

Anderson, M. G., and Burt, T. R.: The role of topography in controlling throughflow generation, Earth Surf. Process., 3, 331–334, https://doi.org/10.1002/esp.3290030402, 1978.

Beiter, D., Weiler, M., and Blume, T.: Characterising hillslope–stream connectivity with a joint event analysis of stream and groundwater levels, Hydrol. Earth Syst. Sci., 24, 5713-5744, https://doi.org/10.5194/hess-24-5713-2020, 2020.

Bishop, K., Seibert, J., Nyberg, L., and Rodhe, A.: Water storage in a till catchment. II: Implications of transmissivity feedback for flow paths and turnover times, Hydrol. Process., 25, 3950-3959, https://doi.org/10.1002/hyp.8355, 2011.

Cui, Z., Tian, F., Zhao, Z., Xu, Z., Duan, Y., Wen, J., and Khan, M. Y. A.: Bimodal Hydrographs in Semi-humid Forested Watershed: Characteristics and Occurrence Conditions, Hydrol. Earth Syst. Sci. Discuss., https://doi.org/10.5194/hess-2024-36, 2024.

Dang, L., Xie, Y. Q., Wang, C., Chang, Y., Zeng, X. K., and Wu, J. C.: Precipitation-induced Pressure Wave Propagation in Unsaturated Zone and Its Effect on Rapid Groundwater Discharge, Geol. J. China Univ., 29,

580-589, https://doi.org/10.16108/j.issn1006-7493.2021104, 2023.

Detty, J. M., and McGuire, K. J.: Threshold changes in storm runoff generation at a till-mantled headwater catchment, Water Resour. Res., 46, W07525, https://doi.org/10.1029/2009WR008102, 2010.

Farrick, K. K., and Branfireun, B. A.: Soil water storage, rainfall and runoff relationships in a tropical dry forest catchment, Water Resour. Res., 50, 9236-9250, https://doi.org/10.1002/2014WR016045, 2014.

Graeff, T., Zehe, E., Reusser, D., Lück, E., Schröder, B., Wenk, G., John, H., and Bronstert, A.: Process identification through rejection of model structures in a mid-mountainous rural catchment: observations of rainfall-runoff response, geophysical conditions and model inter-comparison, Hydrol. Process., 23, 702–718, https://doi.org/10.1002/hyp.7171, 2009.

Graham, C. B., and McDonnell, J. J.: Hillslope threshold response to rainfall: (2) development and use of a macroscale model, J. Hydrol., 393, 77–93, https://doi.org/10.1016/j.jhydrol.2010.03.008, 2010.

Graham, C. B., Woods, R. A., and McDonnell, J. J.: Hillslope threshold response to rainfall: (1) A field based forensic approach, J. Hydrol., 393, 65–76, https://doi.org/10.1016/j.jhydrol.2009.12.015, 2010.

Haga, H., Matsumoto, Y., Matsutani, J., Fujita, M., Nishida, K., and Sakamoto, Y.: Flow paths, rainfall properties, and antecedent soil moisture controlling lags to peak discharge in a granitic unchanneled catchment, Water Resour. Res., 41, W2179–W2187, https://doi.org/10.1029/2005wr004236, 2005.

Haught, D. R. W. and Meerveld, H. J.: Spatial variation in transient water table responses: differences between an upper and lower hillslope zone, Hydrol. Process., 25, 3866-3877, https://doi.org/10.1002/hyp.8354, 2011.

Hewlett, J. D., and Hibbert, A. R.: Factors affecting the response of small watersheds to precipitation in humid areas, in: Forest Hydrology, edited by: Sopper, W. E. and Lull, H. W., Pergamon Press, Oxford, 275–290, 1967.

Kendall, K. A., Shanley, J. B., and McDonnell, J. J.: A hydrometric and geochemical approach to test the transmissivity feedback hypothesis during snowmelt, J. Hydrol., 219, 188–205, https://doi.org/10.1016/S0022-1694(99)00059-1, 1999.

Kosugi, K., Fujimoto, M., Katsura, S., Kato, H., Sando, Y., and Mizuyama, T.: Localized bedrock aquifer distribution explains discharge from a headwater catchment, Water Resour. Res., 47, W07111, https://doi.org/10.1029/2010WR009884, 2011.

Lundin, L.: Soil moisture and ground water in till soil and the significance of soil type for runoff, PhD Thesis, Uppsala University, UNGI Report No. 56, 216 pp., 1982.

Martínez-Carreras, N., Hissler, C., Gourdol, L., Klaus, J., Juilleret, J., Iffly, J. F., and Pfister, L.: Storage controls on the generation of double peak hydrographs in a forested headwater catchment, J. Hydrol., 543, 255–269, https://doi.org/10.1016/j.jhydrol.2016.10.004, 2016.

McDonnell, J. J., Spence, C., Karran, D. J., Van Meerveld, H. J., and Harman, C. J.: Fill-and-spill: A process description of runoff generation at the scale of the beholder, Water Resour. Res., 57, e2020WR027514, https://doi.org/10.1029/2020WR027514, 2021.

Padilla, C., Onda, Y., and Iida, T.: Interaction between runoff–bedrock groundwater in a steep headwater catchment underlain by sedimentary bedrock fractured by gravitational deformation, Hydrol. Process., 29, 4398–4412,

https://doi.org/10.1002/hyp.10498, 2015.

Penna, D., Tromp-van Meerveld, H. J., Gobbi, A., Borga, M., and Dalla Fontana, G.: The influence of soil moisture on threshold runoff generation processes in an alpine headwater catchment, Hydrol. Earth Syst. Sci., 15, 689-702, https://doi.org/10.5194/hess-15-689-2011, 2011.

Rinderer, M., van Meerveld, I., Stähli, M., and Seibert, J.: Is groundwater response timing in a pre-alpine catchment controlled more by topography or by rainfall? Hydrol. Process., 30, 1036-1051, https://doi.org/10.1002/hyp.10634, 2016.

Scaife, C. I., Singh, N. K., Emanuel, R. E., Miniat, C. F., and Band, L. E.: Non-linear quickflow response as indicators of runoff generation mechanisms, Hydrol. Process., 34, 2949–2964, https://doi.org/10.1002/hyp.13780, 2020.

Sloto, R. A., and Crouse, M. Y.: HYSEP: A computer program for streamflow hydrograph separation and analysis, US Geol. Surv., https://doi.org/10.3133/wri964040, 1996.

Tian, F., Li, H., and Sivapalan, M.: Model diagnostic analysis of seasonal switching of runoff generation mechanisms in the blue river basin, Oklahoma, J. Hydrol., 418-419, 136–149, https://doi.org/10.1016/j.jhydrol.2010.03.011, 2012.

Tromp-van Meerveld, H. J., and McDonnell, J. J.: Threshold relations in subsurface stormflow: 1. A 147-storm analysis of the Panola hillslope, Water Resour. Res., 42, W02410, https://doi.org/10.1029/2004WR003778, 2006a.

Tromp-van Meerveld, H. J., and McDonnell, J. J.: Threshold relations in subsurface stormflow: 2. The fill and spill hypothesis, Water Resour. Res., 42, W02411, https://doi.org/10.1029/2004WR003800, 2006b..

# Appendix A:

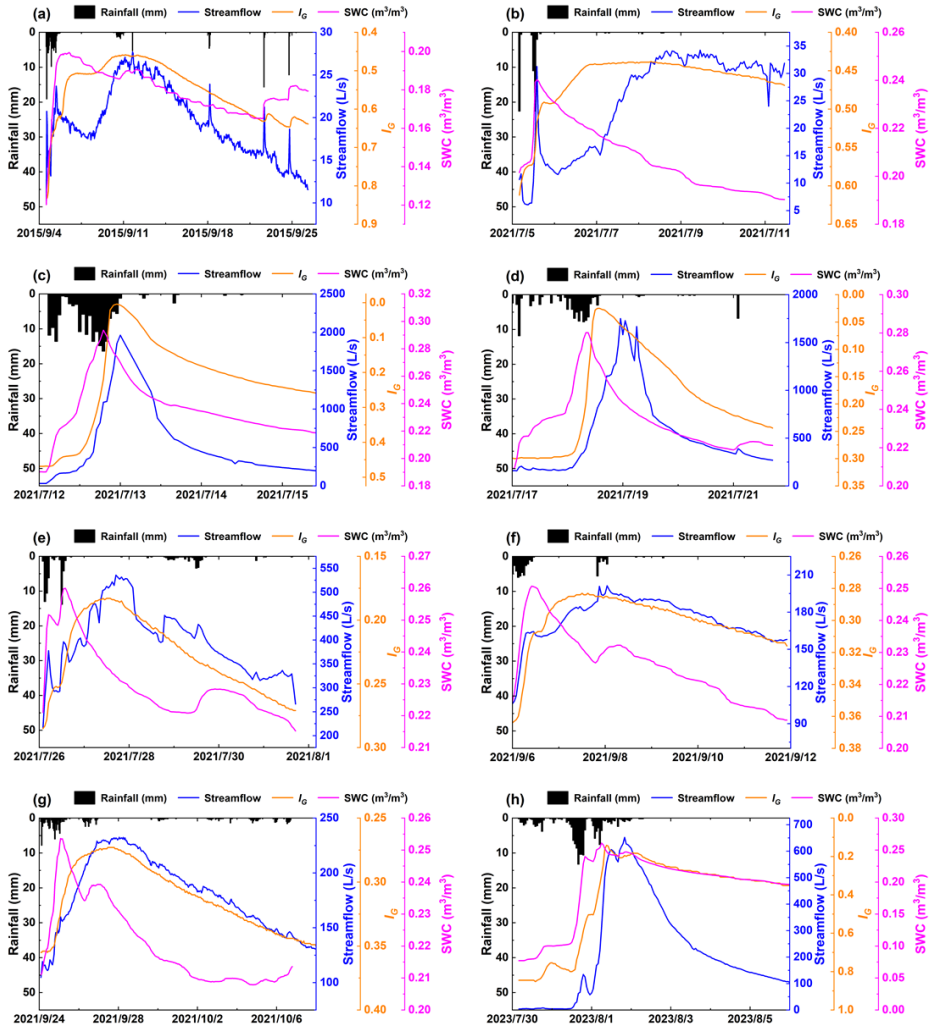


**Figure A1.** Examples of responses of streamflow, $I_G$ and soil water content to rainfall.